

Millimeter-Wave Heating, Radiometry, and Calorimetry of Granite Rock to Vaporization

Paul Woskov · Phil Michael

Received: 10 August 2011 / Accepted: 17 October 2011 /
Published online: 27 October 2011
© Springer Science+Business Media, LLC 2011

Abstract Millimeter-wave (MMW) technologies can provide unique heating and diagnostic capabilities to research the thermal dynamics of materials to extreme temperatures. The MMW properties of rocks in the molten state up to their vaporization temperatures are not well known. Using a 28 GHz gyrotron beam collinear with a 130 GHz radiometry view in a calorimetric chamber, the transitions of granite rock specimens through solid phases, melting, and vaporization were observed, including release of trapped trace gas ($<0.07\%$). The 28 GHz emissivity of molten granite was observed to be approximately constant at 0.66 ± 0.03 up to vaporization where it increased to 0.70 ± 0.03 at an equilibrated temperature of $2710 \pm 120^\circ\text{C}$. An analysis of the thermal power balance during a 76 s steady state vaporization time period indicates that the MMW emissivity of the molten granite is larger than in the infrared. The observations support the possibility that MMW thermal ablative penetration into hot crystalline rock formations could be a more practical approach than infrared laser drilling to access deep resources.

Keywords Gyrotron · Radiometer · Calorimeter · Rock vaporization · Millimeter-wave drilling · Heterodyne receiver · Molten granite · Thermal dynamics · Engineered geothermal systems

1 Introduction

Thermal analysis by MMW radiometry methods [1] can be combined with MMW high power gyrotron radiation [2] to enable unique capability to research the thermodynamic properties of materials to extreme temperatures that have not been accessible to real time dynamic studies in the past. In particular, the properties of rocks melts up to the vaporization temperature can be quantitatively studied. The vaporization parameters of rocks are not readily available expect for a few studies of meteor ablation in the atmosphere [3, 4] and one study of the specific heat of vaporization with a $10 \mu\text{m}$ CO_2 laser [5]. MMW

P. Woskov (✉) · P. Michael
Plasma Science and Fusion Center, Massachusetts Institute of Technology, Cambridge, MA 02139, USA
e-mail: ppwoskov@mit.edu

studies of rock fusion and vaporization have not yet been carried out. However, MMW interactions with rocks at high temperature could be of value for developing new options to access earth's resources such as sustainable geothermal energy [6]. The use of infrared lasers for directed energy penetration of rocks has been researched for many decades without practical realization [7–10]. A fundamental limitation to the use of infrared wavelengths for rock drilling is the inability to effectively couple power to a surface while simultaneously extracting an outward flow of small particles. Short infrared wavelengths are readily scattered by micron and submicron sized particles. Longer MMWs would remove this limitation because small particle Rayleigh scattering losses scale as $1/\lambda^4$. Furthermore, MMW sources are more efficient and have higher average power relative to lasers [11, 12] and can be efficiently guided as a beam over long distances [13] compatible with borehole dimensions. This suggests the economic possibility of completely vaporizing rock to facilitate extraction as a nanoparticle particle smoke. Previous works have shown that solids can be readily ablated to nanoparticles with sufficient heat and gas purge as in meteor ablation [3], nanoparticle manufacturing [14], and welding [15]. In this study we present the first results of using MMWs to melt and vaporize rock, measurements of the MMW emissivity of molten granite and its vaporization temperature.

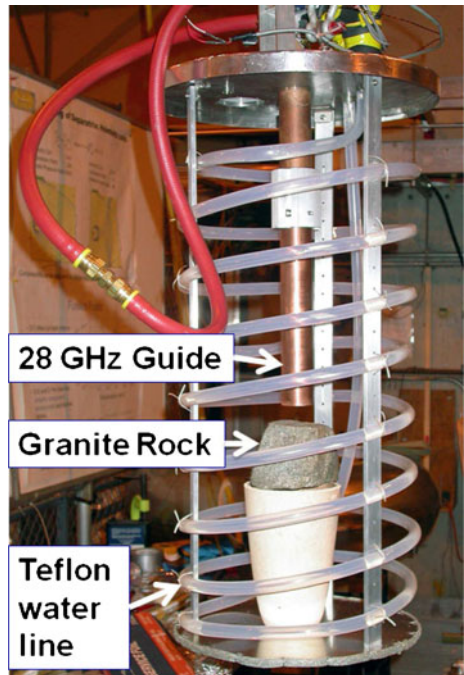
2 Experimental setup

2.1 Test chamber

A 10 kW, 28 GHz CPI Model VIA-301 HeatWave gyrotron was used for the experiments. The gyrotron operates in the second harmonic on the TE_{02} mode which is converted to the TE_{01} mode by an external mode converter [16]. The MMW beam was transmitted in 32 mm i. d. circular copper waveguide in the TE_{01} mode to the rock specimen located inside a water load test chamber. There were two 90° waveguide bends in the transmission line to bring the upward directed beam around and downward toward the test chamber. The test chamber was fashioned from a 32 cm diameter by 76 cm internal height stainless steel Dewar enclosed with a stainless steel lid for trapping all 28 GHz power. The lid and the attached insides of the test chamber are shown in Fig. 1 lifted outside the Dewar enclosure. The waveguide enters from the top through the center of the lid and extends 48 cm into the chamber. The rock samples were typically located within about one waveguide diameter of the launch aperture where the beam has not yet diffracted significantly. The first rock specimen tested is shown in Fig. 1 supported in position on a ceramic crucible. In subsequent tests the crucible was replaced with an aluminum support. A loose helical coil of 1.3 cm diameter Teflon tubing with flowing water lined the inside wall of the chamber to absorb trapped power. Water flow and temperature rise were monitored to determine absorbed power. Without the rock specimen or support this chamber was used to calibrate the gyrotron output power.

Air flow was also introduced into the chamber (not shown in Fig. 1), to exhaust and minimize propagation of volatiles back up the waveguide, through a 2.5 mm diameter nozzle directed across a waveguide barrier window inside the waveguide above the chamber and through a 15 by 3 mm elliptic nozzle blowing across the waveguide aperture at a flow of about $10 \text{ m}^3/\text{hr}$ (see Figs. 5 and 6). The air exhausted through small holes in a 75 mm diameter grill in the lid that prevented 28 GHz leakage. The air exhaust was directed through a 10 cm diameter aluminum duct (see Fig. 2) to a small particle filter and water trap. By measuring the water temperature rise with and without air flow, the presence of the air flow through the chamber was found not to perturb the power measurements.

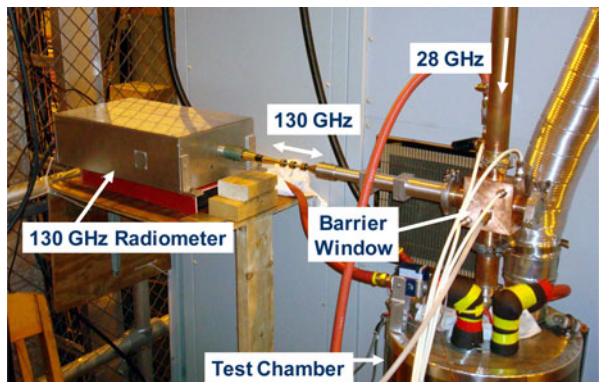
Fig. 1 Internal configuration of rock exposure test chamber with first granite rock before exposure.



2.2 Radiometer diagnostic

Real-time rock surface temperature measurements were made possible with a 130 GHz heterodyne radiometer having 0.5–2.0 GHz sidebands. The experimental arrangement with the radiometer above the test chamber is shown in Fig. 2. The superposition of the radiometer view onto the 28 GHz heating beam was accomplished with a 4-port copper waveguide block that was cut diagonally to hold a fused quartz barrier window at a 45° angle to the waveguide axis. The window was polished to a thickness of 2.90 mm to minimize reflected losses at 28 GHz and to maximize reflection at 130 GHz. Approximately 50% of the radiometer view was reflected downward and >90% of 28 GHz heating beam was transmitted through the barrier window to the test specimen. The

Fig. 2 The 130 GHz MMW radiometer is shown connected to the high power 28 GHz waveguide and test chamber.



waveguide connection from the radiometer to the 4-port block was tapered through small fundamental mode waveguide (WR-6, 1.7×0.8 mm) to cutoff 28 GHz power. The port opposite the radiometer view was shorted with a stainless steel blank flange in the first experiments as shown, and in subsequent experiments a 30 cm long water cooled stainless steel bellows tube was added between the 4-port block and shorting flange to act as a 28 GHz load. The emissivity and temperature of the flange are small relative to the viewed hot test specimen and therefore thermal signal from the flange is not a significant factor. Also calibrations below the barrier window included the radiometer view of the shorting flange while it was still warm after a test.

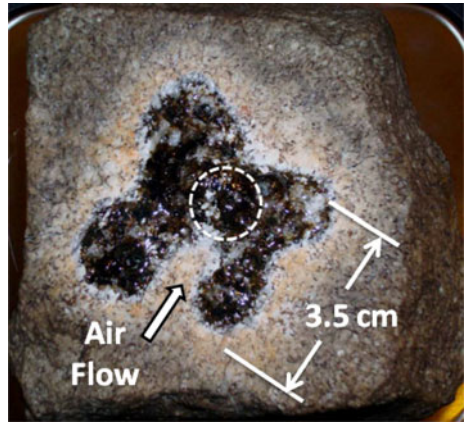
The radiometer itself was a double sideband heterodyne receiver built around a subharmonic mixer and 65 GHz local oscillator from Millitech, Inc. An internal mechanical chopper modulated the radiometer view at about 100 Hz between an internal room temperature reference (Eccosorb [17]) and the sample. A lock-in amplifier referenced to the chopper was used to detect the temperature difference signal. The radiometer does not distinguish between hot or cold temperature differences and therefore a cryogenic source was used to calibrate for hot temperature measurements. The calibration was achieved by removing a short 10 cm long section of the 28 GHz waveguide below the 4-port block after a rock exposure and inserting a known temperature blackbody (liquid nitrogen cooled Eccosorb [17]). In this way all the losses in the tapered waveguide, beamsplitter reflectivity, and blank flange reflection/emission were included in the calibration. The noise temperature of the radiometer at this point was about 20,000 K double sideband therefore keeping both the calibration and measured temperatures ($<2000^\circ\text{C}$) in the linear small signal limit.

3 Experiments

3.1 Rock irradiation

Light gray granite rock commonly found in eastern Massachusetts was studied because it is representative of difficult to penetrate hard crystalline rock types. The 28 GHz index of refraction and absorption coefficient at room temperature were determined by transmission measurements through a 21 mm thick slab cut with parallel surfaces using an Agilent Model E83632B network analyzer. The index of refraction and the absorption coefficient were found to be 2.24 and 0.14 nepers/cm, respectively, corresponding to a $1/e$ propagation depth of 7.1 cm. In Fig. 3 the surface of the first granite specimen tested having a thickness of over 8 cm and weighing 1790 g is shown after two MMW beam exposures: the first for 3.6 minutes at up to 4 kW incident power and then after cool down for another 3.3 minutes at up to 6 kW incident power. The dashed circle with a diameter of 15.5 mm indicates the approximate position of the TE_{01} mode peak power contour on the rock surface 23 mm from the waveguide aperture. The irregular black area shows glass melt that has bubbled up and flowed out from the beam. Many broken bubble craters of up to a maximum diameter 5 mm are present indicating the escape of gases during heating. An incursion of unmelted surface into the black area from the lower left, as shown by the arrow, corresponds to the location of the air flow path across the waveguide aperture. The unmelted surface region immediately around the melted area is lighter in color than the original rock and was found later to be weaker and easily crumbled. Hairline fractures produced by the gyrotron beam exposure also radiated from the melt and extended about 4 cm down each side of the rock specimen.

Fig. 3 Photograph of the surface of the first granite rock specimen tested after up to 6 kW 28 GHz exposure.



A second granite specimen initially weighting 1344 g and over 9 cm thick was also exposed to MMW power that was slowly increased from 1.2 to 3.9 kW over approximately a 9 minute period as described below. The exposure resulted in a similar black glass melt surface area as seen with the first specimen. This rock was cut in half cross the center of the melt area to reveal the depth of the melt and is shown in Fig. 4. The depth of the black melt extends about 9 mm at its maximum. The lighter bleached region extends about 30 mm deep. The fracture extending diagonally downward from the upper left was caused by the heat exposure. Though there may be significant penetration at 28 GHz into the rock at room temperature, at higher temperatures above the melting point the absorption is primarily at the surface.

In a third test with a rock specimen having a surface with a peaked ridge, the ridge was partially ablated away as shown in Fig. 5 with views before and after the gyrotron beam irradiation. This rock was exposed to two pulses of about 5 kW for 50 s each with an average distance of the initial surface peak less than 20 mm from the waveguide aperture.

In a fourth rock exposure experiment, the rock specimen was moved to a distance of 52 mm from the waveguide aperture, allowing the waveguide launched beam to diffract

Fig. 4 Second granite specimen cut open across center of the black melt spot. The depth of the black melt extends about 9 mm at its maximum.



Fig. 5 Before and after photos of third granite specimen with a non-flat surface showing the peaked ridged surface ablated away by the 28 GHz gyrotron beam.



significantly. Shown in Fig. 6, the TE_{01} mode pattern with a power minimum in the center is clearly evident in the melt pattern on the rock surface. At this distance the TE_{01} peak power contour diverges to a diameter of 30 mm. The melt pattern suggests that the beam is skewed to one side, possibly due to some waveguide misalignment. The rock was exposed to a beam power level between 4 and 5 kW for a total time of about 10 minutes over several pulses. The air nozzle that blows across the waveguide aperture to the right of the waveguide is also more distant from the rock surface. Consequently, the rock surface area that appeared bleached white in the other exposures appears reddish here. This coloration of red with distant air flow and white with nearby air flow was consistently observed.

In all the tests, the maximum peak power that could be applied to the rock surface and duration were limited by the reflected power interlock at the gyrotron or arcing at the barrier window after vaporization deposits started to coat the window. In general forward power above 5 kW could not be sustained. The longest continuous exposure of 9 minutes was achieved with the second rock specimen when the forward power was kept below 3 kW for most of that time and then terminated by barrier window arcing due to vaporization deposits after the power was increased to 3.9 kW. Quantitative measurements and modeling of the first two granite specimens are presented in this report.

3.2 Gyrotron forward/ reflected power measurement

The forward and reflected gyrotron powers were monitored by a pair of identical Schottky diode detectors on a TE_{02} forward and backward directional coupler at the gyrotron output. The forward detector was calibrated with the water load test chamber without a rock sample.

Fig. 6 Granite rock surface 52 mm distant from waveguide aperture showing TE_{01} pattern.



present. The reflected power detector was not absolutely calibrated, but its ratio with the forward detector served as an indicator of reflection. The reflection fraction determined in this way cannot be used with the forward power calibration because it ignores mode conversion, waveguide insertion loss, and detector nonlinearity. The waveguide insertion loss and detector nonlinearity would add about 30–40% to the calibration, but mode conversion reflection could be higher.

The forward power and reflected fraction are shown in Fig. 7 without a rock (solid curves) and with the first rock specimen for the two MMW exposures (dashed curves). This data was recorded at a 5 Hz rate and smoothed over a 2 second interval to remove rapid transients. As the gyrotron power is turned on or abruptly increased the reflection fraction starts out high and drifts to lower level over minute time scales. The reflection fraction does not depend on the forward power level. When a rock sample is present in the test chamber the averaged reflected fraction adds about 1 to 2% over the empty chamber reflection which is in itself about 1 to 2% after warm up. For both rock heating periods shown, the gyrotron interlock was tripped by too high a reflection signal on the same detector recorded in Fig. 7b. This was likely caused by a rapid transient not resolved by the data acquisition recording.

3.3 Power and temperature measurements

The MMW thermal emission, forward power and water absorbed power are shown in Figs. 8 and 9 for the first and second heating, respectively, of the first rock specimen tested that resulted in the surface shown in Fig. 3. The forward gyrotron beam power was gradually increased from 2 to 4 kW during 3.6 minutes for the first heating. After about a 30 minute delay the second heating was started with an attempt to switch on to full power of 10 kW, as shown by the spike at about 65 s in Fig. 9, but prevented by the reflected power interlock trip. Subsequently, the power was turned on to an initial 3.75 kW and gradually increased to 6 kW over 3.3 minutes. From these plots the fraction of the forward power not going to the water load due to the presence of the rock can be determined by subtracting the water power from the forward power. The resulting fraction for the second

Fig. 7 Gyrotron forward power (a) and reflected fraction (b) without a rock sample during load calibration (solid lines) and with the first rock sample (dashed) for two heating times. The relative time axes of the data sets were adjusted for clarity of comparison.

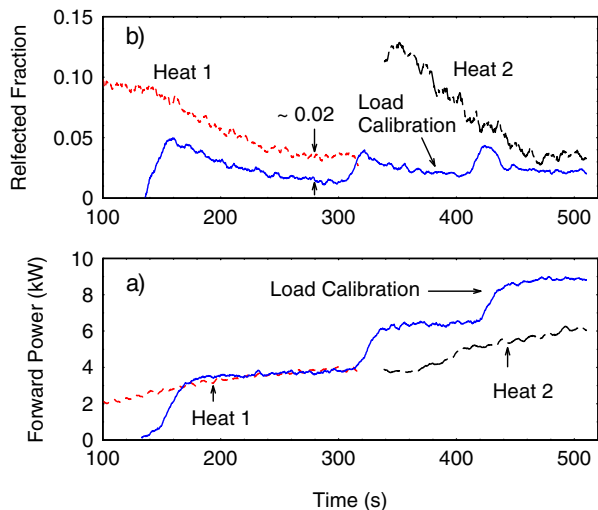
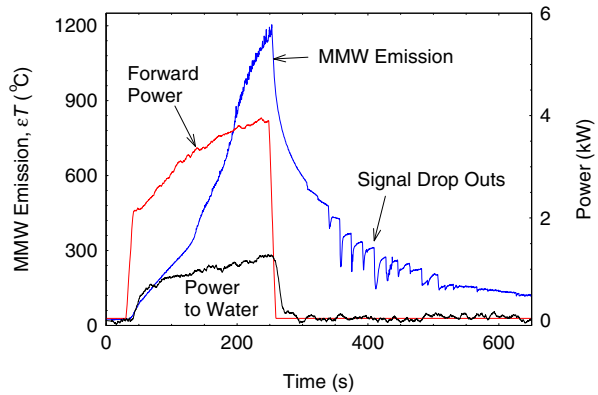


Fig. 8 MMW emission, forward power and water absorbed power for first exposure of rock shown in Fig. 3.



heating is shown in Fig. 10 as a function of the recorded MMW thermal emission, corrected for the slight drift in water power baseline due to the rock warming up. This value on average appears to be constant at 0.69 to the highest melt temperatures observed. The rock absorbed power and consequently the emissivity at 28 GHz can be obtained from this number by subtracting the fraction of power reflected back into the waveguide and not measured by the water load. This puts the emissivity in the range of 0.66 ± 0.03 , assuming that the reflected power into the waveguide could be up to 2 to 3 times higher than the measured TE_{02} reflection shown in Fig. 7. This emissivity is consistent with earlier measurements of 0.64 ± 0.05 at 137 GHz for black glass melt composed of metal oxides found in rocks [18].

The plotted MMW thermal emission signal corresponds to the product of specimen emissivity and temperature (ϵT). Knowledge of the emissivity is important to interpreting the MMW thermal emission plots, which provide unique information on the thermal dynamics of heating the granite to extreme temperatures as well as the temperatures at which key transitions occur. Assuming the 130 GHz radiometer emissivity is in the same range as that obtained here for 28 GHz, the temperature determined from this emissivity is given in parenthesis after the observed MMW emission temperature in the following discussion.

In the first heating shown in Fig. 8, the emissivity corrected initial rate of temperature rise of $7.4 \pm 0.2^{\circ}\text{C/s}$ below 100°C ($151 \pm 6^{\circ}\text{C}$) with 1.3 kW absorbed power is consistent

Fig. 9 MMW emission, forward power and water absorbed power for the second gyrotron beam exposure of the first rock specimen shown in Fig. 3.

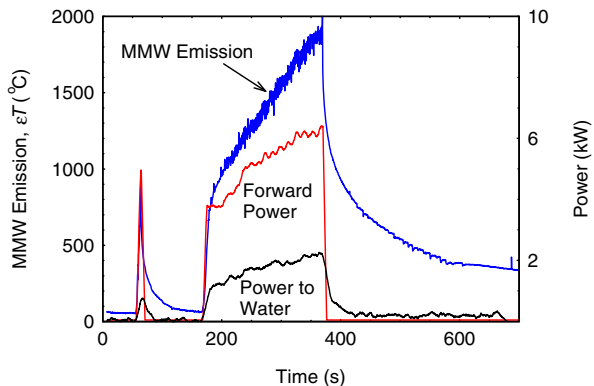
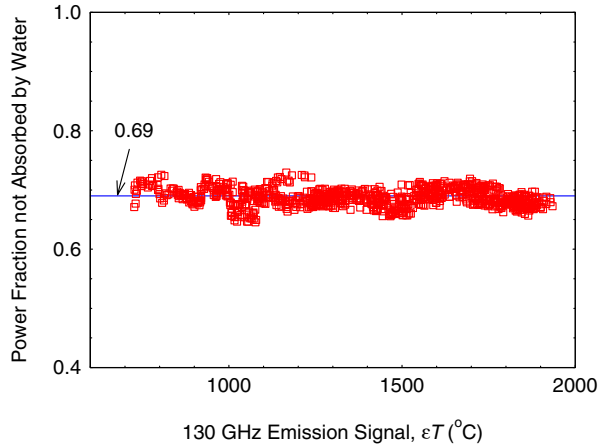


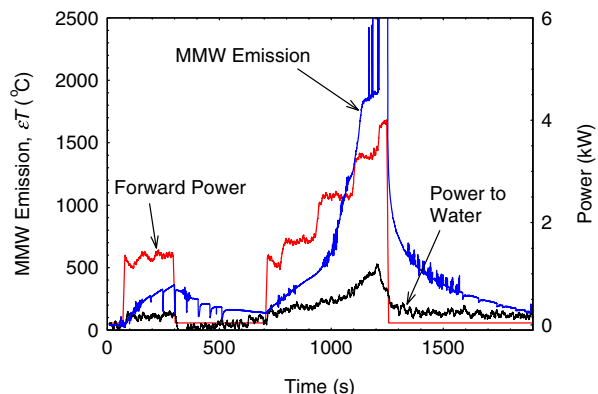
Fig. 10 Fraction of forward power that was not absorbed by the water for the data in Fig. 9 plotted as a function of the MMW thermal emission, ϵT . Twenty point smoothing was used to reduce data scatter.



with the gyrotron beam propagating into the rock to heat a large volume. Granite room temperature heat capacity of 0.8 J/g/K and specific density of 2.7 g/cm^3 [19] would make the volume 82 cm^3 . This is 24% larger than the rock column defined by the waveguide i. d., consistent with beam divergence inside the rock. At higher temperatures, changes in rate of temperature rise that are significantly faster than the slower input power variation suggest phase transitions causing rapid changes in rock opacity and heat capacity. The inflection in MMW emission at about 300°C ($460 \pm 20^\circ\text{C}$) could correspond to the transition to the weaker solid phase that was observed. The change in slope and start of rapid small MMW emission fluctuations at about 820°C ($1235 \pm 45^\circ\text{C}$) likely corresponds to the start of melting, which is in agreement with the published melting range of granite of $1215\text{--}1260^\circ\text{C}$ [20].

Another interesting feature of the MMW emission are signal drop outs during cool down, also observed with the other rock specimens (during both warm up and cool down). These are likely due to thermal induced fracture causing out gassing from the cooler, deeper rock volume by a gas species that is opaque in the radiometer frequency band. This interpretation is supported by the observation that the signal drop outs are not as deep with longer gyrotron beam exposures after the heat penetrates further into the rock heating the gas (evident on the far cool down slope in Figs. 9 & 11, 12). The most likely gas is SO_2

Fig. 11 The complete MMW heating record of the second granite specimen.



which has many rotational transitions spanning the 128–132 GHz radiometer band [21]. This identity for the trace gas release is also supported by a faint burnt match odor observed in the laboratory during some of the tests.

The data for the second heat up of this rock with up to 6 kW forward power is shown in Fig. 9. The initial rate of rock surface temperature rise starting at about 170 s was at an emissivity corrected rate of $110 \pm 5^\circ\text{C/s}$ before beginning to turn over at the melting temperature of about 800°C ($1200 \pm 45^\circ\text{C}$). This is more than an order of magnitude faster than in the first heat up and can be interpreted by the black glass surface that likely resulted from the first exposure as being much more opaque at 28 GHz than the virgin granite. MMW thermal emission increased at an average rate of $8.5 \pm 0.5^\circ\text{C/s}$ above 800°C until a maximum temperature of about 1860°C ($2800 \pm 120^\circ\text{C}$) was reached. The noisy nature of the MMW emission during the melt phase suggests a turbulent molten surface, which was also discernable at a weaker level in Fig. 8.

3.4 Second rock specimen vaporization

The maximum temperature achieved with the first rock specimen was found to correspond approximately to the vaporization temperature when the second granite specimen was tested. The power and temperature record for the second granite rock specimen is shown in Figs. 11, 12. It was initially heated for about 4 minutes at 1.3 kW followed by about a 7 minute cool down and then a 9 minute period when the power was gradually stepped from about 1.2 to 3.9 kW. Transient blockage of the MMW radiometer emission signal is evident during and after the first heating period, as well as weaker events after 1600 s when the specimen was in the final cool down. Dense noise bursts in the MMW emission signal below vaporization temperature are electrical interference during this test. The sudden reduction in MMW temperature rise at about 1100 s is interpreted as the start of the vaporization phase.

Figure 13 is a blow up of the time period of 1000–1300 s around the vaporization time. The upward spikes on the MMW emission indicate barrier window arcing, which became a steady arc when the forward power stepped up to 3.9 kW. The vaporization period was maintained for approximately 76 s at a forward power of 3.4 kW before the final arc. The peak MMW emission appears to have stabilized at 1896°C ($2860 \pm 130^\circ\text{C}$) before the main arc. This is higher than the accepted vaporization temperature of pure silicon dioxide of 2230°C . It was found later that white powder deposits around the contours of the air flow jet on the barrier window caused the arcing. This is consistent with silicon dioxide, which is

Fig. 12 MMW emission, forward power, and water absorbed power for the second rock specimen showing power coupling to rock during vaporization for 76 s and ~ 0.24 kW rock radiation after forward power is turned off.

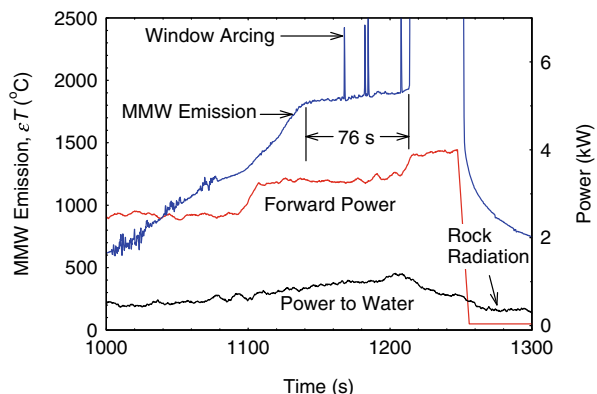
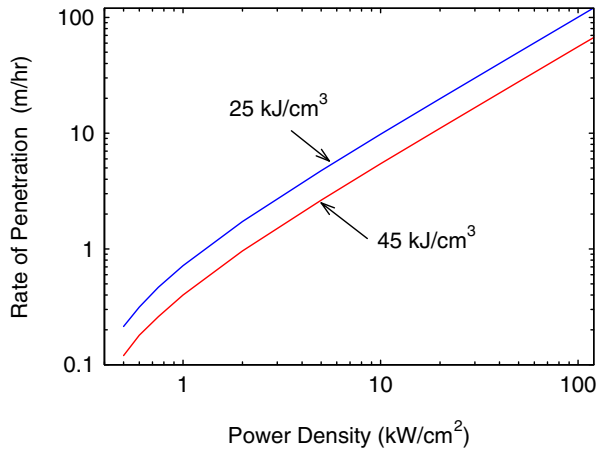


Fig. 13 Vaporization rate of penetration plotted as a function of beam power density for two specific heats of vaporization assuming MMW emissivity of 0.7.



white as a powder and the main constituent (>70%) of granite. At the end of the long gyrotron beam exposure the rock specimen also continued to radiate 0.24 kW for many minutes. Assuming this radiation was ongoing during vaporization and contributing to the water absorbed power indicates that the 28 GHz emissivity increased to about 0.70 ± 0.03 during vaporization. This could be a consequence of the vaporization front softening the surface dielectric boundary reducing reflection loss. A higher continuous vaporization emissivity would also correspond to a lower steady state vaporization temperature of about $2710 \pm 120^\circ\text{C}$.

3.5 Mass losses

The rock specimens were weighed before and after exposure with an A&D-EJ6100 scale. The total mass extracted from the rock samples was very small due to the combination of low power levels and short exposures used for these experiments. The mass loss of the first rock specimen was measured to be 1.2 g or 0.07% of the total rock mass, which can all be attributed to out gassing and not rock vaporization since this specimen was not at the vaporization temperature for any significant time. Also, there was no evidence of vapor deposits on the barrier window or inside waveguide after this first rock test. The mass loss of the second rock was measured to be 3.2 g or 0.24% of the total rock mass of which 2.2 g would correspond to actual rock vaporization, assuming that the measured fraction of out gassing observed with the first specimen holds for the second rock specimen.

4 Discussion

4.1 Power balance

Equating the power input to all the power losses at the granite surface during the steady state vaporization period can be used to determine the specific energy of vaporization of granite if all the power losses can be properly accounted for. The power balance equation can be written as:

$$P_{vap} = \varepsilon P_f - P_{rad} - P_{cond} - P_{conv} \tag{1}$$

where P_{vap} is the vaporization power, P_f is the gyrotron forward power, P_{rad} , P_{cond} , P_{conv} are the radiation, conduction, convection power losses, and ϵ is the MMW emissivity. The forward power during vaporization (3.41 kW) and the MMW emissivity (0.70) corresponds to an absorbed power, ϵP_f , of 2.25 kW. The conduction power loss is also assumed to be 0.24 kW from the measured water load power after gyrotron shut down, which is the result of the rock heated through conduction from the vaporization area assuming warming of the test chamber does not contribute. The other power loss terms are given by:

$$P_{vap} = \frac{sV}{t} \tag{2}$$

$$P_{rad} = \epsilon_{ir} \sigma A (T_h^4 - T_c^4) \tag{3}$$

$$P_{conv} = hA(T_h - T_c) \tag{4}$$

where s is the specific energy of vaporization per unit volume, V is the volume vaporized corresponding to 0.82 cm³ for 2.2 g and a specific density of 2.7 g/cm³, t is the time over which the volume was vaporized (76 s), ϵ_{ir} is the infrared emissivity at peak thermal radiation wavelength (~1 μm at 2700°C), $\sigma = 5.67 \times 10^{-8}$ Wm⁻² K⁻⁴ is the Stefan-Boltzmann constant, A is the vaporization area of 8.0 cm² from the beam area within the melt spot, T_h is the vaporization temperature, T_c is the temperature of the surrounding environment assumed to be 300 K, and h is the convective heat transfer coefficient. It is assumed here that the radiative heat loss is not equilibrated with the water load flow due to the poor infrared reflectivity of the test chamber and poor transmission through the Teflon water tubing.

The convective heat transfer coefficient was estimated to be 56 W/m²/K for the measured air flow and using the air thermal properties found in [22] for laminar flow, which gives a convective heat loss estimate of ~0.1 kW. This leaves 1.91 kW to balance between the vaporization power and radiative power loss, which cannot be done for a positive vaporization power unless the infrared emissivity of molten granite is less than 0.5 at 2710°C.

The infrared emissivity of molten glass varies widely in the literature. For molten commercial clear glass, the infrared emissivity is greater than 0.9 [23]. However, Vakulenko *et al.*, [24] have measured the infrared emissivity of basalt melts to be in the range of 0.2 - 0.5. Also, Abithi *et al.*, [25] have observed that the infrared emissivity of basalt lava decreases with increasing temperature, measuring a value of 0.55 at a temperature of 1050°C. If we assume an infrared emissivity in the range of 0.2- 0.5, then the specific energy of vaporization of our granite sample would fall in the range of 10–100 kJ/cm³. Consequently, an accurate determination of the specific energy of vaporization cannot be obtained by a power balance analysis unless the infrared emissivity of the dominating radiative power loss term is known. Alternatively, a measurement of mass removal with incident beam intensity significantly above the threshold of vaporization would be required.

Previous work to determine the specific heat of vaporization for rocks has resulted in a wide range of values. Calorimetry with a 10 μm CO₂ laser by Bacon *et al.*, [5] showed a 20–100 kJ/cm³ range. Graves *et al.* [8], also using a CO₂ laser, measured a value of ~47 kJ/cm³ for granite. These infrared laser measurements are likely to be high if reflected power is not properly accounted for. Though an accurate determination of the specific energy of vaporization is not possible here, it is evident from the present experiments and analysis that MMWs are better absorbed than infrared radiation by high temperature molten rock.

4.2 Implications for rock drilling

The implications for the performance and economics of MMW directed energy drilling can be estimated from these thermodynamic parameters, assuming practical engineering issues for implementation are resolved. The possible rates of penetration (ROP) as a function of beam power density are plotted in Fig. 13 for a MMW coupling efficiency of 0.7, IR emissivity of 0.5, and for specific energies of vaporization of 25 and 45 kJ/cm³. A practical range of power density would need to be above 1 kW/cm² to significantly exceed radiative heat losses and below 100 kW/cm² to avoid plasma breakdown. Plasma breakdown needs to be avoided because it would result in inefficient omnidirectional heating. The ROP could be as high as 100 m/hr for a specific energy of vaporization near 25 kJ/cm³ and 100 kW/cm² intensity. This would be more than 100 times faster than past experience with engineered geothermal system drilling (EGS) [26]. With 50% efficient, 2 MW gyrotron tubes under development [11], full bore directed energy drilling by vaporization could be achieved with over 1 kW/cm² intensities in borehole diameters of up to 25 cm. Electrical energy costs would be about 7000 kWhr per cubic meter rock mass removed and should remain constant with depth, independent of rock hardness or temperature. These potential ROPs, lower costs, and linear cost scaling are all desirable features being sought for in an EGS drilling technology [6].

5 Conclusions

In conclusion, this work shows that high power MMW sources combined with sensitive MMW diagnostic techniques and calorimetry can be important research tools for studying the thermal dynamics of materials heated to extreme temperatures. Localized heating with the heating beam multiplexed with diagnostics make possible quantitative, moderately rapid heating rate studies to temperatures that otherwise could not be easily achieved. The MMW radiometric granite rock observations identified phase transformations in a few minutes over a wide dynamic range of temperature starting with a weaker solid phase, melting, and finally vaporization with quantified temperatures where transitions occurred. Furthermore, the unique capability to identify trace out gassing by observing spectroscopic absorptions against the intense thermal background produced by the high power MMW beam allows ready access to sensitive studies of gases trapped in rock. This research capability and new data on hard crystalline granite rock should find value in many fields. In particular, the observations reported here show that MMW directed energy would be superior to infrared beams for penetrating hard crystalline rock formations. Not only would the Rayleigh scattering losses scale favorably with wavelength, but the energy balance shows that MMWs are absorbed more efficiently in molten rock than infrared sources such as flames or lasers.

Acknowledgments This work was supported by the MIT Energy Initiative. The authors also acknowledge Richard Latons and Don Strahan for implementing the experimental setup; Robert F. Ellis, Jay Kesner and the LDX team for making the gyrotron available; Richard Temkin for the use of the network analyzer; Dan Cohn and Herbert Einstein for informative discussions.

References

1. P. P. Woskov, S. K. Sundaram, "Thermal return reflection method for resolving emissivity and temperature in radiometric methods", *J. Appl. Phys.*, **92** 6302–6310 (2002).

2. D. Lewis *et al.*, “Materials processing with a High Frequency Millimeter-Wave Source”, *Materials and Manufacturing*, **18** 151–167 (2003).
3. D. M. Hunten, R. P. Turco, O. B. Toon, “Smoke and Dust Particles of Meteoric Origin in the Mesosphere and Stratosphere”, *J. of Atmospheric Sci.*, **38** 1342–1357 (1980).
4. V.A. Bornshten, *Physics of Meteoric Phenomena*, D. Reidel Publishing, Dordrecht, (1983).
5. J. S. Bacon, S. Russell, J. P. Carstens, *Determination of Rock Thermal Properties* UARL Report No. L-911397-4, NTIS AD755218 (1973).
6. J. W. Tester *et al.*, *The Future of Geothermal Energy*, (MIT 2006).
7. W. C. Maurer, *Advanced Drilling Techniques*, Petroleum Publishing Co., Tulsa, Ok, 421–462 (1980).
8. R. M. Graves *et al.*, “Interaction of pulsed CO and CO₂ laser radiation with rocks”, *Proceedings of SPIE*, **4065** 602–613 (2000).
9. M. R. Hallada, R. F. Walter, S. L. Seiffert, “High power laser rock cutting and drilling in mining operations: initial feasibility tests”, *Proceedings of SPIE*, **4184** 590–593 (2001).
10. B. G. Gahan, “Processing Rock”, *Industrial Laser Solutions*, 16–18 (September 2005).
11. M. Thumm, “History, Presence and Future of Gyrotrons”, *IEEE International Vacuum Electronics Conf. (IVEC)*, 37–40 (2009).
12. A. Kasugi, K. Sakamoto, K. Takahashi, K. Kajiwara, N. Kobayashi, “Steady-state operation of 170 GHz- 1 MW gyrotron for ITER”, *Nucl. Fusion*, **48** 054009 (2008).
13. S. T. Han *et al.*, “Low-Power Testing of Losses in Millimeter-Wave Transmission Line for High-Power Applications”, *Intern. J. of Infrared and Millimeter-Waves*, **29** 1011–1019 (2008).
14. R. D. Whitlock and G. M. Frick, “Particle size distributions of aerosols formed by laser ablation of solids at 760 Torr”, *J. Mater. Res.*, **9** 2868–2872 (1994).
15. A. T. Zimmer, “The influence of metallurgy on the formation of aerosols”, *J. of Environ. Monit.*, vol. 4, 628–632, (2002)
16. C. S. Lee, S. W. Lee, S. L. Chuang, “Plot of Modal Field Distribution in Rectangular and Circular Waveguides”, *IEEE Trans. Microwave Theory and Tech.*, **MTT-33** 271–274 (1985).
17. Manufactured by Emerson and Cuming.
18. P. P. Woskov, S. K. Sundaram, W. E. Daniel, Jr., D. Miller, “Molten salt dynamics in glass melts using millimeter-wave emissivity measurements”, *J. of Non Crystalline Solids*, **341/1-3** 21–25 (2004).
19. H. K. Hellwege, Ed., *Landolt-Börnstein Numerical Data and Functional Relationships in Science and Technology*, vol. 1a, Section 4.1, Springer-Verlag, Berlin, (1982).
20. E. S. Larsen, “Temperatures of Magmas”, *American Mineralogist* **14**, 81–94 (1924).
21. S. P. Belov, M. Y. Tretyakov, I. N. Kozin, E. Klisch, G. Winnewisser, W. J. Lafferty, J. M. Flaud, “High Frequency Transitions in the Rotational Spectrum of SO₂”, *J. of Molecular Spectroscopy* **191**, 17–27 (1998). see also www.nist.gov/pml/data/molspec.cfm
22. K.D. Hagen, *Heat Transfer with Applications*, Appendix F, Prentice Hall, Upper Saddle River, New Jersey, (1999).
23. J. L. Berg, “Near Infrared Absorption Coefficient of Molten Glass by Emission Spectroscopy”, *Intern. J. of Thermophysics* **2**, 381–394 (1981).
24. V. O. Vakulenko, D. D. Dzhigiris, Yu. N. Dem’yanenko, B. M. Shutov, “Emmissivity of Basalt Melts”, *Glass and Ceramics* **35**, 530–532 (1979).
25. A.A. Abtahi, A.B. Kahle, A.D. Abbott, A.R. Gillespi, D. Sabol, G. Yamada, D. Pieri, “Emissivity Changes in Basalt After Eruption From PU’UO’O, Kilauea, Hawaii, American Geophysical Union, 2002AGUFM.V71A1263A, (2002).
26. H.C.H. Armstead, J.W. Tester, *Heat Mining*, Chap. 11, E. & F. N. Spon, London, (1987).